Dynamic effects during the capillary rise of fluids in cylindrical tubes

S.B. Lunowa, A. Mascini, C. Bringedal, T. Bultreys, V. Cnudde, I.S. Pop

UHasselt Computational Mathematics Preprint
Nr. UP-21-07

September 8^{th}, 2021

Dynamic effects during the capillary rise of fluids in cylindrical tubes

Stephan B. Lunowa[a,*], Arjen Mascini[b], Carina Bringedal[c], Tom Bultreys[b], Veerle Cnudde[b,d], Iuliu Sorin Pop[a]

[a] *UHasselt – Hasselt University, Computational Mathematics, Agoralaan gebouw D, 3590 Diepenbeek, Belgium*
[b] *Ghent University, Pore-Scale Processes in Geomaterials Research Group (PProGRess), Department of Geology, Krijgslaan 281, 9000 Ghent, Belgium*
[c] *University of Stuttgart, Institute for Modelling Hydraulic and Environmental Systems, Pfaffenwaldring 61, 70569 Stuttgart, Germany*
[d] *Utrecht University, Environmental Hydrogeology Group, Department of Earth Sciences, Princetonlaan 8a, 3584CB Utrecht, The Netherlands*

Abstract

The mathematical models for the capillary-driven flow of fluids in tubes are typically assuming a static contact angle at the fluid-air contact line on the tube walls. However, the dynamic evolution of the fluid-air interface is an important feature during capillary rise. Furthermore, inertial effects are relevant at early times and may lead to oscillations at late times.

To incorporate and quantify the different effects, we start with a fundamental description of the physical processes within the tube. We derive an upscaled model of capillary-driven flow in circular cylindrical tubes that extends the classical Lucas–Washburn theory by incorporating a dynamic contact angle and slip. We further extend this model to account for inertia. Finally, we compare the solutions of the different models to experimental data.

In contrast to the Lucas–Washburn model, the models with dynamic contact angle match the experimental data, both the rise height and the contact angle, even at early times. The models have a free parameter through the dynamic contact angle description, which is fitted using the experimental data. Our findings suggest that this parameter depends only on the properties of the fluid, but is independent of geometrical features, such as the tube radius. Therefore, the presented models can predict the capillary-driven flow in tubular systems upon knowledge of the underlying dynamic contact-angle relation.

Keywords: Capillary rise, dynamic contact angle, upscaling, Lucas–Washburn equation
2008 MSC: 35C20, 76D05, 76D27, 76D45

*Corresponding author.
Email addresses: stephan.lunowa@uhasselt.be (Stephan B. Lunowa), arjen.mascini@ugent.be (Arjen Mascini), carina.bringedal@iws.uni-stuttgart.de (Carina Bringedal), tom.bultreys@ugent.be (Tom Bultreys), veerle.cnudde@ugent.be (Veerle Cnudde), sorin.pop@uhasselt.be (Iuliu Sorin Pop)
URL: orcid.org/0000-0002-5214-7245 (Stephan B. Lunowa), orcid.org/0000-0003-0495-2634 (Carina Bringedal), orcid.org/0000-0001-8217-8053 (Tom Bultreys), orcid.org/0000-0002-3269-5914 (Veerle Cnudde), orcid.org/0000-0001-9647-4347 (Iuliu Sorin Pop)

September 8, 2021

Graphical abstract

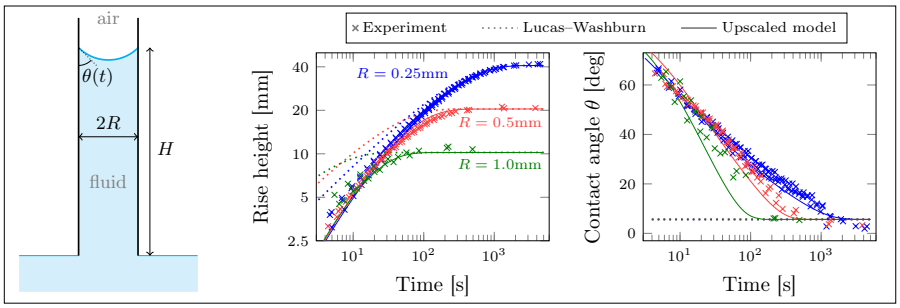

1. Introduction

One hundred years ago, the classical works of Lucas [1], Washburn [2], Rideal [3] and Bosanquet [4] laid the foundation for the description of the capillary-driven flow of fluids in porous structures. Since then, this field of research has gained attention due to its various applications, ranging from water transport in soil and plants, over printing with ink, to oil recovery and CO_2 sequestration. To understand the flow processes in a porous medium, knowledge about the fluid dynamics within its fundamental structures, the single pores, is needed. In these, the surface tension leads to capillary-driven flow. For an overview on the topic, we refer to the recent review by Cai et al. [5].

The model of Lucas and Washburn describes the balance between capillary and hydrostatic pressure, leading to viscous flow until equilibrium at the so-called Jurin's height is reached. Fries and Dreyer [6] derived a formulation for the solution of the Lucas–Washburn equation that remains valid also at late times. Levine et al. [7] studied in detail the resulting flow close to the fluid-air interface, assuming a spherical meniscus and low Reynolds numbers. Although these basic mechanisms are well understood, the complex wetting effects lead to a dynamic evolution of the interface, in particular of both its shape and position. An important feature is the contact angle formed between the fluid-air interface and the pore wall. In the aforementioned works, this contact angle is assumed constant. However, experimental results invalidate this assumption, in particular at early times, see e.g. [8, 9]. Martic et al. [10] discussed this based on molecular dynamics simulations and the molecular kinetics theory. This theory is also used by Hamraoui and Nylander [11] to discuss the effect of a dynamic contact angle as a source of interface retardation and viscous dissipation. Chebbi [12] and Popescu, Ralston and Sedev [13] compare several dynamic contact-angle models when applied to the Lucas–Washburn equation.

Furthermore, inertial effects are relevant for early times of capillary rise, as discussed in detail by Quéré [14], and for low viscous fluids they can even lead to (damped) oscillations around Jurin's height at late times. Xiao, Yang and Pitchumani [15] additionally considered the end effect at the reservoir (sink flow) for parallel plates and tubes, and derived a double Dirichlet series representation

of the solution. An overview of the different regimes has been given by Zhmud, Tiberg and Hallstensson [16] as well as by Fries and Dreyer [17]. However, all these models are based on the assumption of a static contact angle.

To incorporate and quantify the influence of the different effects of the dynamic contact angle and of inertia, one should start with a derivation based on the fundamental description within the tube. The upscaling of the resulting pore-scale solution yields a macroscopic model, which includes the relevant physics and can be validated using experimental data. Thereby, the dynamics of the capillary rise including the detailed evolution of the contact angle become predictable. Furthermore, the application of these extended models helps to reduce the discrepancy between the experiments and classical Lucas-Washburn model observed e.g. in [9].

In this paper, we discuss extended models based on the upscaling of capillary-driven flow in circular cylindrical tubes and validate them by comparison with experimental data. To this end, we model the process by the Navier–Stokes equations in an evolving domain due to the moving fluid-air interface with dynamic contact angle and slip, and apply an asymptotic expansion method. The resulting upscaled model is a nonlinear first-order differential equation of Lucas–Washburn type, which we solve analytically to obtain directly usable solutions. We extend the upscaled model to incorporate inertial effects. The solutions to the upscaled and to the extended model are compared to the experimental results reported by Heshmati and Piri in [9].

The derivation of the solution to the upscaled model for the capillary rise is presented in Section 2, followed by the extension to account for the effect of inertia. To validate the theory, we compare the analytical and numerical solutions to experimental data in Section 3. Finally, the results of the comparison including uncertainties and limitations are discussed in Section 4. More details of the upscaling procedure and of the comparison are presented in Appendix A and Appendix B, respectively.

2. Modeling of capillary rise

We first discuss the upscaled model based on the asymptotic expansion method applied to the Navier-Stokes equations coupled with the fluid-air interface evolution. Thereafter, we extend the model to incorporate inertial effects.

2.1. Upscaled model and analytic solution

We consider the flow of a fluid in a thin, vertical tube, driven by the surface tension at the fluid-air interface. This process can be modeled by the Navier-Stokes equations defined in a time-dependent domain, where the fluid-air interface is a free boundary. Assuming a small Reynolds number, we derive the solution by asymptotic expansion and consider the limit of a vanishing radius-to-length ratio $\varepsilon = R/L$ (R being the tube radius and L Jurin's height). In

the dimensionless form, the evolution of the fluid rise height h is then governed by

$$p_{\text{in}} - h - \frac{8h}{1+4\lambda}\frac{\mathrm{d}h}{\mathrm{d}t} = -\frac{2\cos\left(\theta(\frac{\mathrm{d}h}{\mathrm{d}t})\right)}{\text{Ca}}. \qquad (1)$$

Here p_{in} is the pressure at the inlet (bottom), λ denotes the slip length at the tube wall and Ca is the capillary number, see Figure 1. This equation is derived in Appendix A, where details on the non-dimensionalization and on the asymptotic expansion and the limit $\varepsilon \to 0$ are given. Note that the dynamic contact angle θ may depend on the velocity of the interface. Furthermore, (1) resembles the relation derived by Washburn [2], based on macroscopic arguments. However, Washburn discussed only the case of a static contact angle, while here we incorporate a dynamic contact-angle model.

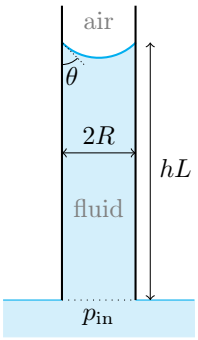

Figure 1: Schematic drawing of the tube with radius R. The contact angle θ is formed between the tube wall and the fluid-air interface at rise height hL. The inlet pressure p_{in} is attained between tube and reservoir.

In the context of capillary rise experiments, the pressure at the inlet is approximately atmospheric, i.e., $p_{\text{in}} = 0$. The typical length scale is given by the equilibrium or Jurin's height $L = 2\sigma\cos(\theta_s)/(\rho g R)$, attained as $t \to \infty$, and which is depending on the fluid-air surface tension σ, the static contact angle θ_s (measured in the fluid), the density ρ of the fluid, the gravitational acceleration $g = 9.81\ \text{m/s}^2$, and the tube radius R. This yields $\text{Ca} = 2\cos(\theta_s)$ (cf. Appendix A), so that (1) becomes

$$\frac{8h}{1+4\lambda}\frac{\mathrm{d}h}{\mathrm{d}t} = \frac{\cos\left(\theta(\frac{\mathrm{d}h}{\mathrm{d}t})\right)}{\cos(\theta_s)} - h, \qquad (2)$$

for all $t > 0$. Clearly,the solution $h = h(t)$ depends on the contact-angle model. However, the specific choice of this model is uncertain without much reference data, since the differences resulting after fitting the different models are typically very small [18, 13]. For simplicity, we consider here a linear model in the velocity, which was also used in [19, 11, 10, 18, 13] as a simplification of the molecular kinetics theory, valid at low velocities. Specifically,

$$\cos(\theta(v)) = \cos(\theta_s) - \eta\text{Ca}v,$$

where the dynamic parameter $\eta \geq 0$ denotes the strength of the linear response due to the interface velocity $v = \frac{\mathrm{d}h}{\mathrm{d}t}$. Note that this model arises naturally for all possible contact-angle models after linearization. With this contact-angle model, the rise model (2) becomes

$$\left(\frac{8h}{1+4\lambda} + 2\eta\right)\frac{\mathrm{d}h}{\mathrm{d}t} = 1 - h, \qquad (3)$$

for all $t > 0$. A natural initial condition is

$$h(0) = 0. \qquad (4)$$

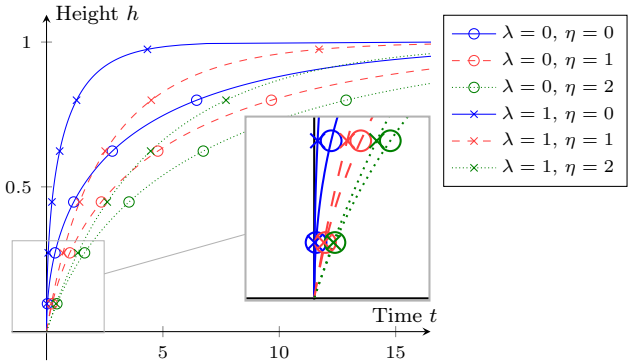

Figure 2: The height of the capillary rise given by (5) increases faster for higher slip length λ. The dynamic parameter η retards the rise and determines the initial velocity at time $t = 0$.

Observe that, since 1 is an equilibrium solution to (3), the solution to the initial value problem (3)–(4) remains below 1 for all times t. Moreover, h is increasing. By separation of variables, the solution to (3)–(4) is obtained in implicit form,

$$(1 - h(t)) \exp\left(\frac{4h(t)}{(1+4\lambda)\eta + 4}\right) = \exp\left(-\frac{(1+4\lambda)t}{2(1+4\lambda)\eta + 8}\right). \tag{5}$$

As h is monotone, using (5) one can express t as a function of h, namely

$$t = t(h) = -\frac{8h}{1+4\lambda} - \frac{2(1+4\lambda)\eta + 8}{1+4\lambda} \ln(1-h).$$

At early times, this yields

$$t \approx 2\eta h + \left(\eta + \tfrac{4}{1+4\lambda}\right) h^2.$$

If $\eta = 0$, this resembles the classical Lucas–Washburn equation. If $\eta > 0$, the first term implies a linear time-height relation at early times, when $h \ll 1$, and therefore quadratic terms can be neglected. Figure 2 illustrates possible solutions. The dynamic parameter η determines the velocity of the rise in the beginning, since (3) yields $\frac{\mathrm{d}h}{\mathrm{d}t}(0) = \frac{1}{2\eta}$. In particular, it is singular if $\eta = 0$, since inertial terms and the movement of the air are neglected. On the other hand, the influence of the slip length λ on the velocity increases with increasing height h. Furthermore, for $\eta > 0$, this yields an initial contact angle $\theta = 90°$ at time $t = 0$.

2.2. Extended model including inertial effects

The upscaled model described above requires the Reynolds number to be small. In case of a low viscosity, or when the tube radius increases, the Reynolds number becomes large, so that we cannot neglect inertial effects. In that situation, the upscaling procedure does not yield a closed expression for the height

of the capillary rise, as the system remains fully coupled. Instead, we suggest to use an empirical extension of the upscaled model, based on macroscopic considerations, as discussed in [4, 16, 11, 17]. There, the balance between hydrostatic, inertial and capillary forces was considered assuming Hagen–Poiseuille flow and a spherical meniscus. In our context, the resulting balance reads

$$\mathcal{I}\frac{\mathrm{d}}{\mathrm{d}t}\left(h\frac{\mathrm{d}h}{\mathrm{d}t}\right)+\left(\frac{8h}{1+4\lambda}+2\eta\right)\frac{\mathrm{d}h}{\mathrm{d}t}=1-h, \tag{6}$$

where $\mathcal{I}=\varepsilon^2\mathrm{Re}=\rho^3g^2R^5/(2\mu^2\sigma\cos(\theta_s))$ is the inertial coefficient, see Appendix A. Note that the denominator $(1+4\lambda)$ accounts for slip, and the term $2\eta\frac{\mathrm{d}h}{\mathrm{d}t}$ is due to the linearized contact-angle model.

With (4), this nonlinear second-order differential equation becomes degenerate. Furthermore, one needs to specify a second initial condition, similar to the initial velocity. Like in [16], we use an asymptotic analysis carried out for $t\to 0$ with ansatz $h(t)=ct^\alpha+o(t^\alpha)$. Equating the leading order terms, we obtain that $h(t)\sim t/(\eta+\sqrt{\eta^2+\mathcal{I}})$, and hence

$$\left.\frac{\mathrm{d}h}{\mathrm{d}t}\right|_{t=0}=\frac{1}{\eta+\sqrt{\eta^2+\mathcal{I}}}. \tag{7}$$

To solve the initial value problem (4), (6), and (7) numerically, we reformulate it as a system of nonlinear first-order differential equations and use the variables $w:=h^2$ and $v:=\frac{\mathrm{d}w}{\mathrm{d}t}$ to the planar system. Equation (6) then becomes

$$\frac{\mathrm{d}w}{\mathrm{d}t}=v,\qquad \frac{\mathrm{d}v}{\mathrm{d}t}=\frac{2}{\mathcal{I}}\left(1-\sqrt{w}-\left(\frac{4}{1+4\lambda}+\frac{\eta}{\sqrt{w}}\right)v\right).$$

To avoid the singularity at $w=0$, we use the initial conditions $w(0)=10^{-12}$ and $v(0)=2\sqrt{w(0)}(\sqrt{\eta^2+\mathcal{I}}-\eta)/\mathcal{I}$. Note that this choice does not significantly affect the result as long as $w(0)$ is sufficiently small. We have implemented the numerical solver in Python 3.8.10 using the packages `NumPy` 1.21.0 [20], and `SciPy` 1.3.3 [21]. The chosen time integrator is an implicit multi-step variable-order (1–5) BDF method. The source code is available in [22].

3. Comparison with experimental data

To validate the suggested models, we compare the solutions to the experimental data reported by Heshmati and Piri in [9], where the capillary rise of glycerol, Soltrol 170 and water in vertical glass tubes with constant radii was investigated. These results include both the rise height and of the contact angle over time.

The comparison is done in three steps. First, the physical properties reported in [9] are used for the dimensionless scaling, see also Table 1. Second, we assume the late-time data to be near to equilibrium, and extract from these the static contact angle for each of the three fluids. Note that the resulting

Fluid	ρ [kg/m^3]	μ [Pa s]	σ [N/m]	R [mm]	θ_s [deg]
Glycerol	1260	1.0111	0.06346	0.250, 0.500, 1.00	5.63
Soltrol 170	774	0.0026	0.02483	0.375, 0.500, 0.65	9.79
Water	997	0.0011	0.0728	0.375, 0.500, 0.65	9.99

Table 1: The density ρ, viscosity μ, surface tension σ of the fluids and the experimental tube radii R, as reported in [9]. The static contact angle θ_s is extracted from the late-time data.

static angles ($<10°$) hardly influence the rise height ($<2\%$), but strongly affect the dynamic contact angle. In the third step, we match the solutions of the suggested models to the experimental data by fitting the remaining parameters; namely the dynamic contact-angle parameter η and the slip length λ. For this, for each fluid and each radius separately, we perform a non-linear least-squares fitting of the rise height ("h-fit"), of the contact angle ("θ-fit"), and of both at the same time ("both-fit"). Thereby, we can compare the parameter values obtained for the different fits as well as for the different radii, to investigate the predictive abilities of the suggested models. We have implemented the procedure in Python 3.8.10 using the packages `pandas` 1.3.0 [23] and `LMFIT` 1.0.2 [24]. The source code is available in [22].

To illustrate the effect of the dynamic contact-angle model, we also provide the classical Lucas–Washburn solution, which is obtained from (5) when taking $\eta = 0$ and $\lambda = 0$, using the dimensionless scaling and static contact angle found in the first and second step for the comparison.

3.1. Glycerol

In the first set of measurements, glycerol was used as the rising fluid. The parameters are given in Table 1. The scale ratio ε was below 0.1 for all radii. Due to the high viscosity, the inertial effects are negligible ($\mathcal{I} < 1.5 \cdot 10^{-3}$), so that the solutions to the upscaled model (5) and to the extended one (6) coincide. Therefore, we present in Table 2 only the results for the upscaled model. Note that the simultaneous fitting of the parameters η and λ results in dimensionless slip lengths $\lambda < 10^{-2}$, except for the both-fit at the radius 1.0mm, which yields $\lambda = 0.026 \pm 0.109$. Hence, slip is negligible and ignored in the further discussion.

The comparison of the experimental data with the fitted upscaled model (3) and the classical Lucas–Washburn model ($\eta = 0$) in Figure 3 illustrates the relevance of the dynamic contact angle. While both models match the late-time data when the static contact angle is approached, only the upscaled model with dynamic contact angle agrees with the early-time data. In particular, it matches reasonably both the rise height and the contact angle for all three radii. Note that the three fit-types (h, θ, both) yield different parameters, but the resulting solutions only differ on the scale of the scatter in the experimental data, see also Appendix B. Note that the increase in η with increasing radius is expected,

R	h-fit		θ-fit		both-fit	
[mm]	η	χ^2_ν	η	χ^2_ν	η	χ^2_ν
0.25	0.402 ± 0.010	0.059	0.525 ± 0.008	0.647	0.519 ± 0.006	0.388
0.50	2.356 ± 0.066	0.327	2.151 ± 0.069	2.105	2.183 ± 0.049	1.203
1.00	5.935 ± 0.383	1.226	10.077 ± 0.613	3.985	8.787 ± 0.461	4.053

Table 2: The best-fit parameter η (± estimated standard deviation) and the reduced residual χ^2_ν when fitting the upscaled model to the experimental data of the height (h-fit), the contact angle (θ-fit) and both (both-fit), for the glycerol experiments.

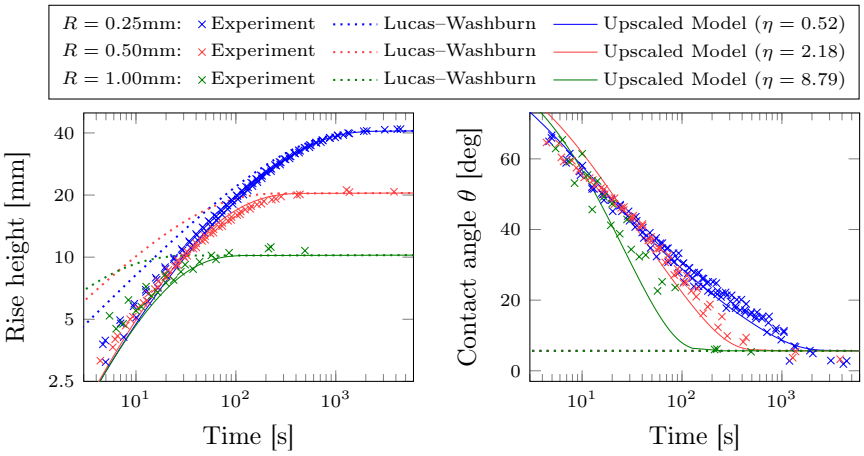

Figure 3: The experimental data for glycerol is matched well by the upscaled model (both-fit). In particular, at early times the representation of the rise is much better than the one for the classical Lucas–Washburn model.

as the dimensional dynamic parameter should be approximately constant. This effect is discussed for all fluids in Section 4.1.

3.2. Soltrol

In the second set of measurements, Soltrol 170 was used as the rising fluid. The parameters are given in Table 1. The scale ratios ε were below 0.1 for all radii. In contrast to the previous case, the extended model differs from the upscaled one ($\mathcal{I} = 1.0$, 4.2, 15.7), but for all radii the best-fit parameters coincide within 1.5 standard deviations ($< 5\%$ difference), while the residuals are rather lower (-40% to $+30\%$ difference, avg. -6%). Hence, we illustrate the minor differences in Figure 4, and report the results for both models in Table 3. Note that the fit of the dimensionless slip length yields $\lambda < 10^{-6}$ in all cases, which is again negligible and thus ignored.

For Soltrol, the fitted upscaled model (5) matches the experimental data almost perfectly, while the classical Lucas–Washburn model ($\eta = 0$) only predicts

R	h-fit		θ-fit		both-fit	
[mm]	η	χ^2_ν	η	χ^2_ν	η	χ^2_ν
0.375	1.464 ± 0.067	0.313	1.250 ± 0.058	2.153	1.273 ± 0.042	1.232
0.500	2.521 ± 0.080	0.196	2.358 ± 0.081	1.042	2.386 ± 0.056	0.603
0.650	4.588 ± 0.162	0.414	3.963 ± 0.143	1.370	4.098 ± 0.108	0.951
0.375	1.437 ± 0.005	0.340	1.241 ± 0.027	2.239	1.261 ± 0.044	1.275
0.500	2.430 ± 0.075	0.207	2.309 ± 0.062	0.623	2.330 ± 0.045	0.403
0.650	4.370 ± 0.016	0.537	3.830 ± 0.024	1.183	3.944 ± 0.122	0.899

Table 3: The best-fit parameter η (± estimated standard deviation) and the reduced residual χ^2_ν when fitting the upscaled model (*top rows*) and the extended model (*bottom rows*) to the experimental data of the height (h-fit), the contact angle (θ-fit) and both (both-fit), for the Soltrol 170 experiments.

R	h-fit		θ-fit		both-fit	
[mm]	η	χ^2_ν	η	χ^2_ν	η	χ^2_ν
0.375	0.162 ± 0.005	0.058	0.377 ± 0.017	2.054	0.367 ± 0.013	1.143
0.500	0.111 ± 0.020	0.153	0.498 ± 0.037	3.914	0.476 ± 0.026	2.249
0.650	2.849 ± 0.064	0.234	1.052 ± 0.079	4.595	1.248 ± 0.079	4.203

Table 4: The best-fit parameter η (± standard deviation) and the reduced residual χ^2_ν when fitting the extended model (without slip) to the experimental data of the height (h-fit), the contact angle (θ-fit) and both (both-fit), for the water experiments.

the stationary solution well (see Figure 4). In particular, the upscaled model with dynamic contact angle agrees with the data of both the rise height and the contact angle for all three radii and at all times. For more details, see also Appendix B. The fit of the extended model coincides with the one of the upscaled model. Only at very early times (until 0.05s), the extended model predicts a slightly lower contact angle. These early-time dynamics are especially relevant for larger radii and less viscous fluids like water, as we show in the following and discuss in Section 4.

3.3. Water

In the last set of measurements, distilled water was used as the rising fluid. The parameters are given in Table 1. The scale ratios ε were below $2.9 \cdot 10^{-2}$ for all radii. In contrast to the previous cases, the extended model differs significantly from the upscaled one ($\mathcal{I} = 4.1, 17, 64$), see Figure 5. The upscaled model (both-fit) only matches the contact angle and late-time height (after ≈ 0.05s). The experimental data is much better represented by the extended model, hence we only report these results in Table 4. More details and the results of the upscaled model can be found in Appendix B. Note that the fit of the dimensionless slip length was inconsistent ($\lambda < 0.15$) with generally large standard deviation.

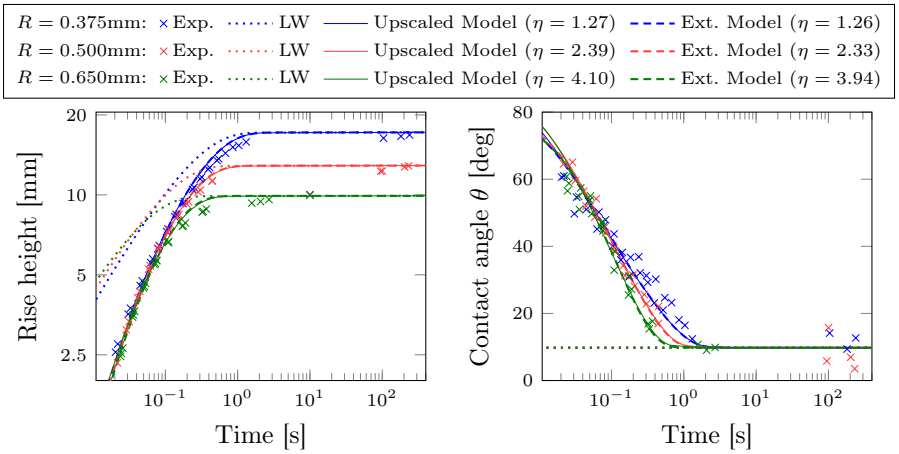

Figure 4: The experimental data for Soltrol 170 is matched almost perfectly by the upscaled model (both-fit), while the classical Lucas–Washburn model (LW) only describes the stationary solution well (after 1s). For the upscaled and the extended models after fitting, the solutions practically coincide.

For the θ-fits, the slip was negligible ($\lambda < 10^{-9}$), while the other fits suggest the occurrence of an effective slip, which might be due to pre-wetting films, as discussed in Section 4.4.

For water, the fitted extended model matches reasonably the experimental data, although the rise height is slightly over-predicted (+10%) for the radius $R = 0.65$mm, see Figure 5. In particular, note that the model predicts an overshoot (between 0.2s and 0.4s). The experimental data does not show this behavior. Instead, the rise seems delayed compared to the other experiments (3.4mm vs. 6.5–7.4 at time 0.016s).

4. Discussion

The above comparison shows that the presented models predict the dynamics of the capillary rise in circular tubes well. In the following, we elaborate on the physical basis of the fitted dynamical parameter, and discuss further aspects that might have an impact on the experimental and theoretical data. In particular, we consider the influence of the initial transient regime and of the meniscus shape, as well as possible wetting films and resulting slip in the case of water. Finally, we address the uncertainty and limitations of the suggested models and of the fitting.

4.1. The dynamic parameter as physical property

The dynamic parameter η obtained by fitting can be interpreted as a physical property of the fluid system. For this, we use dimensional quantities denoted

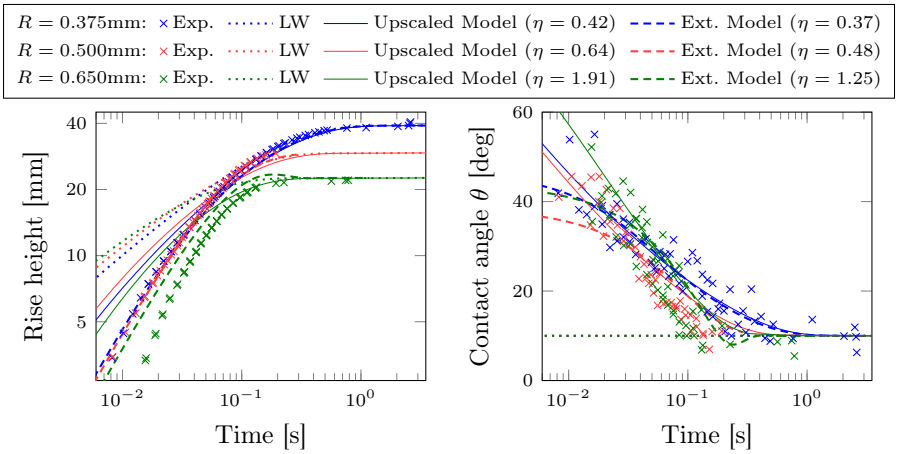

Figure 5: The experimental data for water is matched well by the extended model (both-fit), while the upscaled model (both-fit) only matches the contact angle and late-time data (after ≈ 0.05s). The classical Lucas–Washburn (LW) model only describes the stationary solution well (after 0.1s).

by a hat. Although the different fitting criteria, namely the height, the contact angle, or both, provide optimal parameters with significant variation, the dynamic parameter $\hat{\eta}$ [s/m] (scaling $\mu/(\rho g R^2)$) seems to be independent of the tube radius, see Figure 6. This agrees with the results reported in [19, 11], where the Lucas–Washburn equation with dynamic contact angle was compared with experiments of ethanol, water and silicon oil in glass tubes, and those obtained by molecular dynamics simulations in [10]. Further experimental data considering a larger range of radii and hence velocities is necessary to confirm this hypothesis.

Note that the closely related linearized molecular-kinetic theory discussed e.g. in [19, 10, 11, 18] yields the dynamic contact-angle model

$$\cos(\theta_s) - \cos(\theta) = \xi \hat{v},$$

where $\hat{v}$ denotes the contact line velocity. Here, the intrinsic friction coefficient ξ [s/m] is proportional to the ratio μ/σ of the viscosity to the fluid-air surface tension. Therefore, we expect an almost constant ratio $\hat{\eta}\sigma/\mu$ for all fluids, which is also found for the fitted parameter $\hat{\eta}$, since the ratio is ca. 30–70 for glycerol, ca. 25–35 for Soltrol 170 and ca. 5–50 for water.

4.2. The influence of the initial transient regime

At the start of the experiment, the tube touches the surface of the fluid in the reservoir. This topological change initiates the rise and the meniscus shape, which are hence strongly affected by the (touch) speed and the exact (nanometric) surface of the tube tip. In the suggested models, we neglect this initial transient regime and assume that a stable Hagen–Poiseuille flow profile

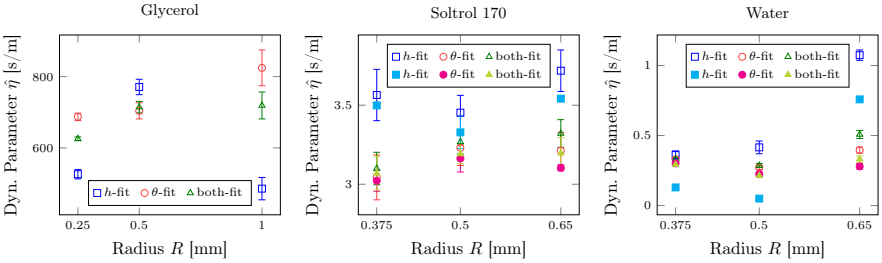

Figure 6: The dimensional dynamic parameter $\hat{\eta} = \eta/U$ of the models (*empty*: upscaled, *filled*: extended) fitted to the experimental data of the height (h-fit), the contact angle (θ-fit) and both (both-fit). Observe that these parameters vary significantly from one fluid to another, but appear to not depend on the tube radius.

and a spherical meniscus are formed quasi-instantaneously. To understand the details better, accurate micro-scale analysis and simulations in the initial stage are necessary. For micro-gravity experiments, Stange, Dreyer and Rath [25] found three successive phases: a quadratic dependence of the meniscus height on time ($h \sim t^2$), followed by a linear increase ($h \sim t$), and, finally, the Lucas–Washburn behavior ($h^2 \sim t$).

However, the fitting results suggest that the initial transient regime is indeed negligible here, especially for glycerol and Soltrol 170 (cf. Sections 3.1 and 3.2), for which we could even neglect inertia (which was included only in the extended model). Nevertheless, for large radii, as well as less viscous fluids, such as water, these effects might be significant. In particular, the water experiment with largest radius ($R = 0.65$mm) shows deviations from an initially linear height-time relation, see Figures 5 and B.13. Additionally, for such regimes, the proper choice of the (numerical) initial conditions for the extended model (6) might be important. Here, we used asymptotic analysis to approach $t = 0$, and a sufficiently small numerical regularization with negligible impact on the solution (cf. Section 2.2). Further investigation can lead to conditions (or extensions) that include the transient effect.

4.3. The meniscus shape

The meniscus shape is assumed spherical for the experimental measurement of the contact angle, as well as for the discussed models. However, this shape might be deformed due to the influence of the inertia and gravity. For glycerol and Soltrol 170, the agreement of the experimental contact-angle data and the fitted upscaled model gives confidence that these effects can be neglected. For water, the experimental contact angle data has a rather large scatter, and the differences between experiments and fitted models are higher (cf. Figures 5 and B.11 to B.13). For experiments with water in glass tubes of lower radius ($R = 0.15$mm and $R = 0.2$mm), Xue et al. [8] reported that the rise velocity is too high to have a spherical meniscus shape. Therefore, the obtained results for the contact angle of water should be treated with caution.

4.4. Wetting films and slip

For glycerol and Soltrol 170, Heshmati and Piri vacuum-dried the tubes immediately before the experiments [9], so that no pre-wetting films were present. Our model fitting resulted accordingly in negligible slip lengths, $\lambda < 10^{-2}$, which translates into a dimensional slip length below 1μm. On the contrary, the tubes for the experiments with water were only partially dried using a paper filter, to avoid a contamination affecting the contact angle and the equilibrium rise [9]. Hence, heterogeneous pre-wetting films of water could possibly be present in the tubes. This can influence the contact angle and the meniscus shape, and induces difficulties for the measurements and the modeling, so that a direct comparison becomes more involved.

Additionally, the presence of wetting films would reduce the dissipation from the formation of water-glass interfacial area. Hence, the water rises faster, which corresponds to an effective slip in our models. In the fitting of the extended model using the height data (h-fit & both-fit), we, indeed, observed a relevant slip length up to 0.15 (dimensional about 0.1mm, cf. Table B.6). However, the dynamic coefficient η and the slip length λ are strongly correlated, such that the slip length in the model is difficult to relate to the physical behavior.

4.5. Uncertainty and limitations of the suggested models and of the fitting

Since the suggested models are derived in leading order for $\varepsilon \ll 1$, errors in the order of ε are expected (here $\varepsilon < 0.01$). Furthermore, for simplicity, we chose a linearized dynamic contact-angle model. A higher accuracy can be obtained using a more sophisticated contact-angle model, which, itself, needs further investigation and validation (cf. [18, 13]). Additionally, a Hagen–Poiseuille flow is assumed for the extended model. Deviations due to inertial effects are ignored, but might affect the inertial coefficient $\mathcal{I}$. This could explain the overshoot observed for the extended model in the case of water with tube radius $R = 0.65$mm (cf. Figure 5), which is not present in the experiment.

Furthermore, the static contact angle is highly sensitive to the used materials. In contrast to the total wetting ($\theta = 0°$) used in [9], we extracted them from the experiments and found values between 5 and 10 degrees. Note that, for water-air-glass systems, even a static contact angle of 20–30 degrees is reported in [26]. Although this has only a minor influence on the rise height, it affects the fitting for the dynamic contact angle.

5. Conclusions

The upscaled model of capillary-driven flow in circular cylindrical tubes extends the classical Lucas–Washburn theory by incorporating a dynamic contact angle. Using a simple relation between the contact angle and the velocity of the moving contact line, we derived an analytical expression for the capillary rise over time. Based on empirical arguments, we extended the mathematical model to account for inertial effects.

To validate the models, we compared the solutions to the experimental data observed by Heshmati and Piri [9]. In contrast to the Lucas–Washburn model, the models with dynamic contact angle do match the experimental data, both the rise height and the contact angle, even at early times. The fitting procedure requires only one parameter for the dynamic contact angle. In particular, our findings suggest that this parameter depends only on the physical properties of the involved fluids (and of the tube), but is independent of geometrical features, such as the radius of the tube. Therefore, the presented models can be used to predict capillary-driven flow in tubular systems upon knowledge of the underlying dynamic contact-angle relation.

In a future work, we will include this approach in a dynamic pore-network model, to study the resulting dynamic core-scale effects and to derive upscaled models valid a that and possibly larger scale.

Data availability statement

The data that support the findings of this study was generated using the source code in [22], which is openly available in GitHub at `https://github.com/s-lunowa/dynamic-capillary-rise`.

Acknowledgments

We are grateful to Mohammad Heshmati and Mohammad Piri for providing their experimental data. We thank the German Research Foundation (DFG) for supporting this work by funding the Collaborative Research Center on Interface-Driven Multi-Field Processes in Porous Media (SFB 1313, grant number 327154368).

Funding

This work was supported by the Research Foundation Flanders (FWO) [grant numbers G051418N, G0G1316N, 12X0919N] and the Hasselt University [project number BOF17NI01]; Tom Bultreys is a postdoctoral fellow of the Research Foundation Flanders.

CRediT author statement

S.B. Lunowa: Conceptualization, Data curation, Formal analysis, Investigation, Methodology, Software, Validation, Visualization, Writing - original draft. **A. Mascini:** Conceptualization, Methodology, Investigation, Validation, Writing - review & editing. **C. Bringedal:** Conceptualization, Methodology, Writing - review & editing. **T. Bultreys:** Conceptualization, Funding acquisition, Writing - review & editing. **V. Cnudde:** Conceptualization, Funding acquisition, Writing - review & editing. **I.S. Pop:** Conceptualization, Funding acquisition, Methodology, Writing - review & editing.

References

[1] R. Lucas, Über das Zeitgesetz des kapillaren Aufstiegs von Flüssigkeiten, Kolloid-Zeitschrift 23 (1918) 15–22. doi:10.1007/BF01461107.

[2] E. W. Washburn, The dynamics of capillary flow, Phys. Rev. 17 (1921) 273–283. doi:10.1103/PhysRev.17.273.

[3] E. K. Rideal, CVIII. On the flow of liquids under capillary pressure, The London, Edinburgh, and Dublin Philosophical Magazine and Journal of Science 44 (1922) 1152–1159. doi:10.1080/14786441008634082.

[4] C. H. Bosanquet M.A., LV. On the flow of liquids into capillary tubes, The London, Edinburgh, and Dublin Philosophical Magazine and Journal of Science 45 (1923) 525–531. doi:10.1080/14786442308634144.

[5] J. Cai, T. Jin, J. Kou, S. Zou, J. Xiao, Q. Meng, Lucas–Washburn equation-based modeling of capillary-driven flow in porous systems, Langmuir 37 (2021) 1623–1636. doi:10.1021/acs.langmuir.0c03134.

[6] N. Fries, M. Dreyer, An analytic solution of capillary rise restrained by gravity, J. Colloid Interface Sci. 320 (2008) 259–263. doi:10.1016/j.jcis.2008.01.009.

[7] S. Levine, J. Lowndes, E. J. Watson, G. Neale, A theory of capillary rise of a liquid in a vertical cylindrical tube and in a parallel-plate channel: Washburn equation modified to account for the meniscus with slippage at the contact line, J. Colloid Interface Sci. 73 (1980) 136–151. doi:10.1016/0021-9797(80)90131-9.

[8] H. T. Xue, Z. N. Fang, Y. Yang, J. P. Huang, L. W. Zhou, Contact angle determined by spontaneous dynamic capillary rises with hydrostatic effects: Experiment and theory, Chem. Phys. Lett. 432 (2006) 326–330. doi:10.1016/j.cplett.2006.10.017.

[9] M. Heshmati, M. Piri, Experimental investigation of dynamic contact angle and capillary rise in tubes with circular and noncircular cross sections, Langmuir 30 (2014) 14151–14162. doi:10.1021/la501724y.

[10] G. Martic, F. Gentner, D. Seveno, D. Coulon, J. De Coninck, T. D. Blake, A molecular dynamics simulation of capillary imbibition, Langmuir 18 (2002) 7971–7976. doi:10.1021/la020068n.

[11] A. Hamraoui, T. Nylander, Analytical approach for the Lucas–Washburn equation, J. Colloid Interface Sci. 250 (2002) 415–421. doi:10.1006/jcis.2002.8288.

[12] R. Chebbi, Dynamics of liquid penetration into capillary tubes, J. Colloid Interface Sci. 315 (2007) 255–260. doi:10.1016/j.jcis.2007.06.073.

[13] M. N. Popescu, J. Ralston, R. Sedev, Capillary rise with velocity-dependent dynamic contact angle, Langmuir 24 (2008) 12710–12716. doi:10.1021/la801753t.

[14] D. Quéré, Inertial capillarity, Europhys. Lett. 39 (1997) 533–538. doi:10.1209/epl/i1997-00389-2.

[15] Y. Xiao, F. Yang, R. Pitchumani, A generalized analysis of capillary flows in channels, J. Colloid Interface Sci. 298 (2006) 880–888. doi:10.1016/j.jcis.2006.01.005.

[16] B. V. Zhmud, F. Tiberg, K. Hallstensson, Dynamics of capillary rise, J. Colloid Interface Sci. 228 (2000) 263–269. doi:10.1006/jcis.2000.6951.

[17] N. Fries, M. Dreyer, The transition from inertial to viscous flow in capillary rise, J. Colloid Interface Sci. 327 (2008) 125–128. doi:10.1016/j.jcis.2008.08.018.

[18] T. D. Blake, The physics of moving wetting lines, Journal of Colloid and Interface Science 299 (2006) 1–13. doi:10.1016/j.jcis.2006.03.051.

[19] A. Hamraoui, K. Thuresson, T. Nylander, V. Yaminsky, Can a dynamic contact angle be understood in terms of a friction coefficient?, J. Colloid Interface Sci. 226 (2000) 199–204. doi:10.1006/jcis.2000.6830.

[20] C. R. Harris, K. J. Millman, S. J. van der Walt, R. Gommers, et al., Array programming with NumPy, Nature 585 (2020) 357–362. doi:10.1038/s41586-020-2649-2.

[21] P. Virtanen, R. Gommers, T. E. Oliphant, M. Haberland, et al., SciPy 1.0: Fundamental Algorithms for Scientific Computing in Python, Nature Methods 17 (2020) 261–272. doi:10.1038/s41592-019-0686-2.

[22] S. B. Lunowa, Software for fitting the upscaled and extended model of capillary rise to experimental data (Sep. 2021).
URL https://github.com/s-lunowa/dynamic-capillary-rise

[23] J. Reback, jbrockmendel, W. McKinney, J. Van den Bossche, et al., pandas-dev/pandas: Pandas 1.3.0 (Jul. 2021). doi:10.5281/zenodo.5060318.

[24] M. Newville, R. Otten, A. Nelson, A. Ingargiola, et al., lmfit/lmfit-py 1.0.2 (Feb. 2021). doi:10.5281/zenodo.4516651.

[25] M. Stange, M. E. Dreyer, H. J. Rath, Capillary driven flow in circular cylindrical tubes, Phys. Fluids 15 (2003) 2587–2601. doi:10.1063/1.1596913.

[26] X. Li, X. Fan, S. Brandani, Difference in pore contact angle and the contact angle measured on a flat surface and in an open space, Chem. Eng. Sci. 117 (2014) 137–145. doi:10.1016/j.ces.2014.06.024.

[27] S. B. Lunowa, C. Bringedal, I. S. Pop, On an averaged model for immiscible two-phase flow with surface tension and dynamic contact angle in a thin strip, Stud. Appl. Math. 147 (2021) 84–126. doi:10.1111/sapm.12376.

[28] C. Huh, L. E. Scriven, Hydrodynamic model of steady movement of a solid/liquid/fluid contact line, J. Colloid Interface Sci. 35 (1971) 85–101. doi:10.1016/0021-9797(71)90188-3.

Appendix A. Summary of the upscaling process for a tube

We consider a three-dimensional thin tube of length L and radius $R \ll L$, see Figure 1, and assume axisymmetry for all quantities. Using a cylindrical coordinate system, we denote the axial and radial component of a vector by $\cdot_z$ and $\cdot_r$ and suppress any dependency on the angular component. We consider the flow of one fluid bounded by a fluid-air interface in contact with the solid tube wall. Following the non-dimensional modeling in [27], due to axial symmetry, the non-dimensional tube is reduced to the domain $\Omega = (0,1)^2$, with scaled differential operators

$$\nabla^\varepsilon = \boldsymbol{e}_z\partial_z + \varepsilon^{-1}\boldsymbol{e}_r\partial_r, \quad \Delta^\varepsilon = \partial_z^2 + \varepsilon^{-2}r^{-1}\partial_r(r\partial_r),$$
$$\mathbf{D}^\varepsilon(\boldsymbol{u}^\varepsilon) = \tfrac{1}{2}(\nabla^\varepsilon \boldsymbol{u}^\varepsilon + (\nabla^\varepsilon \boldsymbol{u}^\varepsilon)^T).$$

The fluid-air interface has an a-priori unknown location and shape at time $t > 0$, and therefore appears as a free boundary in the mathematical model. It is parametrized by $\boldsymbol{\gamma}^\varepsilon = \boldsymbol{\gamma}^\varepsilon(t,s)$, such that the interface at time t becomes $\Gamma^\varepsilon(t) = \{\boldsymbol{\gamma}^\varepsilon(t,s) \mid s \in [0,1]\}$. In particular, $s = 0, 1$ correspond to the interface position in the center and at the tube wall (contact line), respectively. Hence, the normal and tangential unit vectors at $\Gamma^\varepsilon(t)$ are given by

$$\boldsymbol{t}_\Gamma^\varepsilon = \frac{1}{\sqrt{(\partial_s\gamma_z^\varepsilon)^2+(\varepsilon\partial_s\gamma_r^\varepsilon)^2}}\partial_s\boldsymbol{\gamma}^\varepsilon, \quad \boldsymbol{n}_\Gamma^\varepsilon = \frac{1}{\sqrt{(\partial_s\gamma_z^\varepsilon)^2+(\varepsilon\partial_s\gamma_r^\varepsilon)^2}}(\varepsilon\partial_s\gamma_r^\varepsilon\boldsymbol{e}_z - \partial_s\gamma_z^\varepsilon\boldsymbol{e}_r).$$

The flow of one fluid phase is described by the incompressible Navier-Stokes equations (without angular flow),

$$\varepsilon^2\mathrm{Re}\big(\partial_t\boldsymbol{u}^\varepsilon + (\boldsymbol{u}^\varepsilon\cdot\nabla^\varepsilon)\boldsymbol{u}^\varepsilon\big) + \nabla^\varepsilon p^\varepsilon - \varepsilon^2\,\Delta^\varepsilon\boldsymbol{u}^\varepsilon = -\boldsymbol{e}_z \qquad \text{in } \Omega^\varepsilon(t), \tag{A.1}$$
$$\nabla^\varepsilon\cdot\boldsymbol{u}^\varepsilon = 0 \qquad \text{in } \Omega^\varepsilon(t), \tag{A.2}$$
$$p^\varepsilon = p_{\mathrm{in}}, \quad u_r^\varepsilon = 0 \qquad \text{at } z = 0, \tag{A.3}$$
$$u_r^\varepsilon = 0, \quad \partial_r u_z^\varepsilon = 0, \quad \partial_r p^\varepsilon = 0 \qquad \text{at } r = 0, \tag{A.4}$$
$$u_r^\varepsilon = 0, \quad u_z^\varepsilon + 2\varepsilon\lambda^\varepsilon\boldsymbol{e}_z\cdot\mathbf{D}^\varepsilon(\boldsymbol{u}^\varepsilon)\boldsymbol{e}_r = 0 \qquad \text{at } r = 1, \tag{A.5}$$
$$\partial_s\gamma_z^\varepsilon = 0 \qquad \text{at } s = 0, \tag{A.6}$$
$$\cos\big(\theta(\partial_t\gamma_z^\varepsilon)\big) = \boldsymbol{t}_\Gamma^\varepsilon\cdot\boldsymbol{e}_z \qquad \text{at } s = 1, \tag{A.7}$$

where $\boldsymbol{u}^\varepsilon(t,\boldsymbol{x})$ and $p^\varepsilon(t,\boldsymbol{x})$ are the velocity and the pressure of the fluid, which flows inside the domain $\Omega^\varepsilon(t)$. The dimensionless numbers and physical parameters are given in Table A.5. Note that the Navier-slip condition (A.5) is

Parameter	Symbol
Tube length & radius	L & R
Density of the fluid	ρ
Viscosity of the fluid	μ
Surface tension coefficient	σ
Gravitational acceleration	g

Dim.-less Number	Symbol	Value
Scale ratio	ε	R/L
Reynolds number	Re	$\rho^2 g R^2 L/\mu^2$
Capillary number	Ca	$\rho g R L/\sigma$

Dimensionless quantity	Symbol	Scaling
Position	$\boldsymbol{x}$	$[L,\, R]$
Time	t	$\mu L/(\rho g R^2)$
Velocity of the fluid	$\boldsymbol{u}$	$\rho g R^2/\mu$
Pressure of the fluid	p	$\rho g L$
Interface parametrization	$\boldsymbol{\gamma}$	$[L,\, R]$
Interface curvature	κ	$1/R$
Slip length	λ	R
Contact angle law	θ	1

Table A.5: Summary of all parameters (*top left*), dimensionless numbers (*bottom left*), dimensionless quantities and their respective scaling (*right*).

necessary to avoid a singularity in the pressure and in the shear stress at the contact line [28]. Furthermore, the contact angle $\theta : \mathbb{R} \to (0, \pi)$ (measured in the fluid) is given by a dynamic model that depends on the velocity of the contact line.

At the interface $\Gamma^\varepsilon(t)$, the normal stress is balanced by the surface tension,

$$-p^\varepsilon \boldsymbol{n}_\Gamma^\varepsilon + 2\varepsilon^2\, \mathbf{D}^\varepsilon(\boldsymbol{u}^\varepsilon)\boldsymbol{n}_\Gamma^\varepsilon = \tfrac{2}{\mathrm{Ca}}\kappa^\varepsilon \boldsymbol{n}_\Gamma^\varepsilon \qquad \text{on } \Gamma^\varepsilon(t), \tag{A.8}$$

where $\kappa^\varepsilon = \varepsilon\, \nabla^\varepsilon \cdot \boldsymbol{n}_\Gamma^\varepsilon$ is the local mean curvature of the interface. In the normal direction, the interface moves with the fluid,

$$\partial_t(\gamma_z^\varepsilon \boldsymbol{e}_z + \varepsilon \gamma_r^\varepsilon \boldsymbol{e}_r) \cdot \boldsymbol{n}_\Gamma^\varepsilon = \boldsymbol{u}^\varepsilon \cdot \boldsymbol{n}_\Gamma^\varepsilon \qquad \text{on } \Gamma^\varepsilon(t). \tag{A.9}$$

The initial conditions for the interface position and for the velocity are left out here. In the following, we implicitly require them to match the asymptotic solutions, to avoid possible initial layer solutions for small times.

For the following analysis, we use an asymptotic expansion technique with respect to ε. Letting $\varepsilon \to 0$, we derive the formal limit of the model in (A.1)–(A.9), which is which is similar to saying that the tube becomes very thin. The outcome is an upscaled model, which describes the averaged behavior of the system. This is done in two steps, directly following the derivation in [27] for a two-dimensional thin strip. First, we solve the problem in the bulk domain $\Omega^\varepsilon(t)$ away from the interface $\Gamma^\varepsilon(t)$. We then show that this bulk solution has a boundary layer solution in an $\mathcal{O}(\varepsilon)$-region around $\Gamma^\varepsilon(t)$. Altogether, the solution is of Hagen-Poiseuille type in the bulk, coupled by a dynamic Young-Laplace law at the interface, where the interface position and the total flux are given by differential algebraic equations.

All variables are assumed to be smooth and to depend regularly on ε, starting

with the leading order $\mathcal{O}(\varepsilon^0)$. We apply the homogenization ansatz

$$\begin{aligned}\boldsymbol{u}^\varepsilon(t,\boldsymbol{x}) &= \boldsymbol{u}^0(t,\boldsymbol{x}) + \varepsilon\boldsymbol{u}^1(t,\boldsymbol{x}) + \mathcal{O}(\varepsilon^2),\\ p^\varepsilon(t,\boldsymbol{x}) &= p^0(t,\boldsymbol{x}) + \varepsilon p^1(t,\boldsymbol{x}) + \mathcal{O}(\varepsilon^2),\\ \boldsymbol{\gamma}^\varepsilon(t,s) &= \boldsymbol{\gamma}^0(t,s) + \varepsilon\boldsymbol{\gamma}^1(t,s) + \mathcal{O}(\varepsilon^2).\end{aligned}$$

Furthermore, the following assumptions are made on the model parameters.

(H1) The Reynolds number Re is uniformly bounded, i.e., $\mathrm{Re} \leq \mathcal{O}(\varepsilon^0)$.

(H2) The slip length λ^ε has the form

$$\lambda^\varepsilon(t,z) = \lambda^0 + \lambda_e \exp\left(-\varepsilon^{-1}|z - \gamma_z^\varepsilon(t,1)|\right),$$

for given constants $\lambda^0, \lambda_e \geq 0$ that are independent of ε. Moreover, there holds either $\lambda_e = 0$, or $\lambda^0 = 0$. Note that the latter represents the case of rapidly decaying slip away from the interface.

(H3) The contact-angle model $\theta : \mathbb{R} \to (0,\pi)$ is Lipschitz-continuous and does not dependend on ε.

(H4) The leading order interface position in z is constant, i.e., $\partial_s \gamma_z^0 \equiv 0$.

(H5) The capillary number Ca is of order 1, i.e., $\mathrm{Ca} = \mathcal{O}(\varepsilon^0)$.

As will be seen below, (H1) ensures that the flow remains laminar. The independence of ε of θ, as stated in (H3), is crucial for the derivation. As discussed above, the slip is necessary to allow the movement of the contact point. For simplicity, (H2) requires a simple expression of the slip. This avoids technical complexities, while allowing for the typical no-slip condition at the tube wall further away from the interface ($\lambda^0 = 0$). Furthermore, note that (H4) means that the fluid-air interface $\Gamma^\varepsilon(t)$ has only "small" deformations in the order of the radius, i.e., it is almost transversal, such that $\gamma_z^\varepsilon(t,s) = \gamma_z^0(t) + \mathcal{O}(\varepsilon)$.

The asymptotic expansions are used in the flow equations (A.1)–(A.9). Next, the terms of the same order in ε are equated to obtain the limit equations. Note that we are only interested in the leading order terms and relations, therefore higher order terms are neglected. To simplify the notation, the indices $(\cdot)^\varepsilon$ and $(\cdot)^0$ are left out. Hence, all following equations should be understood as up to terms of order ε.

First, we consider the flow in the bulk domain $\Omega^\varepsilon(t)$ and solve the resulting equations away from the interface, using (H1)–(H4) and (A.1)–(A.5). Using the mass conservation (A.2) and the boundary conditions (A.4) and (A.5), one obtains (in the leading order) $u_r = 0$ for $z < \gamma_z(t)$. The second component of the momentum balance (A.1) yields in leading order $\partial_r p = 0$. Integrating the first component of the momentum balance (A.1) twice over r and using the symmetry and the wall boundary conditions (A.4) and (A.5), one obtains

$$u_z(t,\boldsymbol{x}) = \frac{r^2 - (1+2\lambda)}{4}\left(\partial_z p(t,\boldsymbol{x}) + 1\right) \qquad \text{for } z < \gamma_z(t). \tag{A.10}$$

Integrating (A.10) over the cross-section yields

$$q(t) := 2\pi \int_0^1 u_z(t, \boldsymbol{x}) r dr = -\frac{\pi(1+4\lambda)}{8} \left(\partial_z p(t, \boldsymbol{x}) + 1\right), \tag{A.11}$$

for any $z < \gamma_z$, where $q(t)$ denotes the total flux in the tube. Observe that $q(t)$ is independent of z due to the mass conservation (A.2). We obtain the pressure p from (A.11) using the inlet boundary condition (A.3). Inserting the result into (A.10), we obtain the bulk solution

$$p(t, \boldsymbol{x}) = p_{\text{in}}(t) - z - \frac{8z}{\pi(1+4\lambda)} q(t), \quad \boldsymbol{u}(t, \boldsymbol{x}) = 2q(t) \frac{1 + 2\lambda - r^2}{\pi(1+4\lambda)} \boldsymbol{e}_z. \tag{A.12}$$

Note that the solution in the bulk domain is of Hagen-Poiseuille type. In the following, the total flux q will be determined via the boundary layer at the interface $\Gamma^\varepsilon(t)$.

We continue the analysis for the interface region around $\Gamma^\varepsilon(t)$ and insert the homogenization ansatz into (A.1)–(A.9), using (H1)–(H5) and the inner scaling

$$X_z(t, z) := \frac{z - \gamma_z^0(t)}{\varepsilon}, \quad X_r := r, \quad P(t, \boldsymbol{X}) := p(t, \boldsymbol{x}).$$

Then, (A.1) yields in leading order $\nabla_{\boldsymbol{X}} P = \boldsymbol{0}$, so that, by matching with the outer solution, we obtain the constant pressure $P(t, \boldsymbol{X}) = p(t, \gamma_z(t))$. Plugging this into the interfacial stress balance (A.8) yields in leading order that the curvature is constant. Therefore, the interface is a spherical cap. Combining this with the contact-angle condition (A.7), and plugging in the bulk pressure solution (A.12), one obtains

$$p_{\text{in}} - \gamma_z - q \frac{8\gamma_z}{\pi(1+4\lambda)} = -\frac{2\cos\left(\theta(\partial_t \gamma_z)\right)}{\text{Ca}}. \tag{A.13}$$

Using the mass conservation (A.2), the interface velocity (A.9), the outer velocity solution (A.12) and the Gauß theorem, we obtain

$$\begin{aligned} 0 &= \int_{\Omega^\varepsilon} \nabla^\varepsilon \cdot \boldsymbol{u}^\varepsilon d\boldsymbol{x} = \int_{\Gamma^\varepsilon} \boldsymbol{u}^\varepsilon \cdot \boldsymbol{n}_\Gamma^\varepsilon da - 2\pi \int_0^1 u_z^\varepsilon\big|_{z=0} r dr = \pi \int_0^1 \partial_t \gamma_z ds - q \\ &= \pi \partial_t \gamma_z - q. \end{aligned}$$

Therefore, the leading order position γ_z of the interface satisfies

$$\partial_t \gamma_z(t) = \frac{q(t)}{\pi}. \tag{A.14}$$

Inserting this into (A.13) finally yields

$$p_{\text{in}} - \gamma_z - \frac{8\gamma_z}{1+4\lambda} \partial_t \gamma_z = -\frac{2\cos\left(\theta(\partial_t \gamma_z)\right)}{\text{Ca}}.$$

After solving this nonlinear first-order differential equation for the interface position γ_z, the total flux q, the velocity $\boldsymbol{u}$ and the pressure p inside the tube are determined by (A.12) and (A.14). Finally, note that the interface position γ_z is called rise height h throughout the paper.

Appendix B. Detailed results of the fitting

The results of the different fitted models are presented in the following. First, in Figure B.7 we illustrate the different fits of the upscaled model obtained for glycerol. The fits of the upscaled and the extended model for Soltrol 170 are presented in Figures B.8 to B.10. Finally, the fits of the two models for water are presented in Table B.6 and Figures B.11 to B.13, including the results for the simultaneous fit of the dynamic parameter η and the slip length λ.

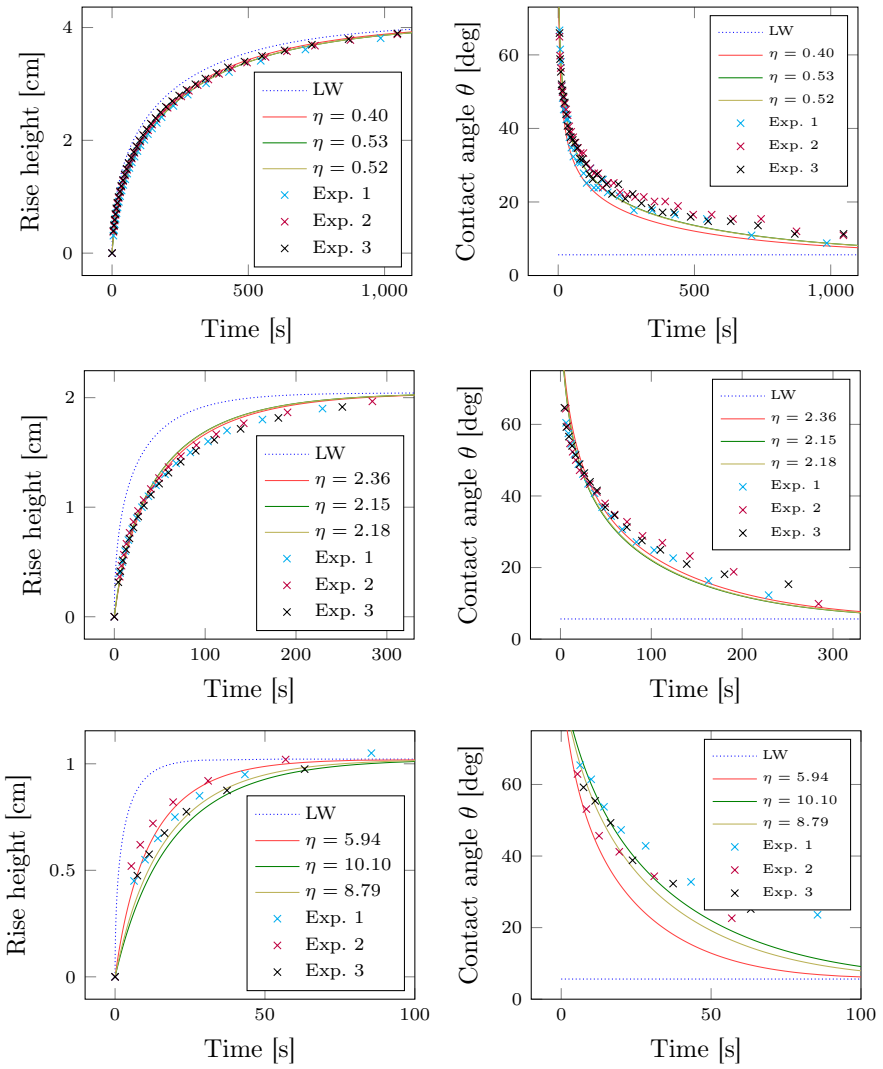

Figure B.7: Simulation results of the Lucas-Washburn model (LW) and of the fitted upscaled model for the glycerol experiments. *Top row:* radius $R = 0.25$mm. *Center row:* radius $R = 0.5$mm. *Bottom row:* radius $R = 1.0$ mm. Red: h-fit; Green: θ-fit; Yellow: both-fit.

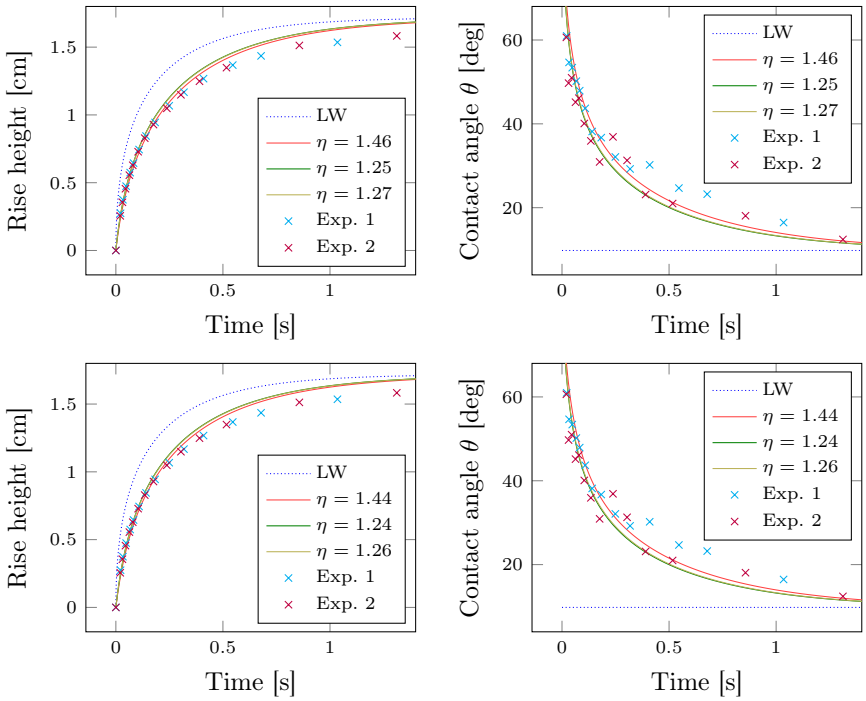

Figure B.8: Simulation results of the Lucas-Washburn model (LW) and of the fitted upscaled (*top row*) and extended (*bottom row*) models for the Soltrol 170 experiments at radius $R = 0.375$mm. Red: h-fit; Green: θ-fit; Yellow: both-fit.

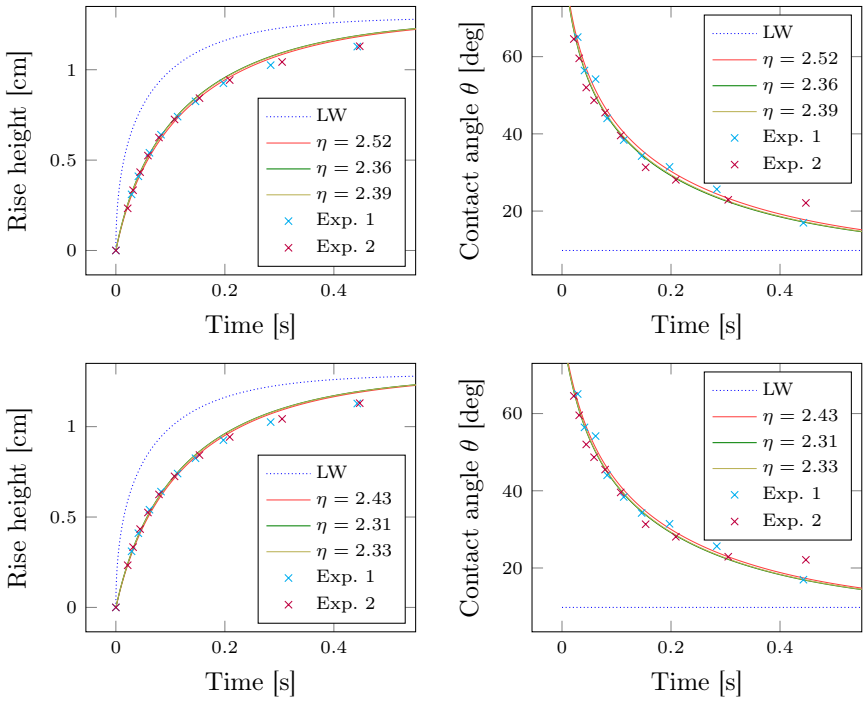

Figure B.9: Simulation results of the Lucas-Washburn model (LW) and of the fitted upscaled (*top row*) and extended (*bottom row*) models for the Soltrol 170 experiments at radius $R = 0.5$mm. Red: h-fit; Green: θ-fit; Yellow: both-fit.

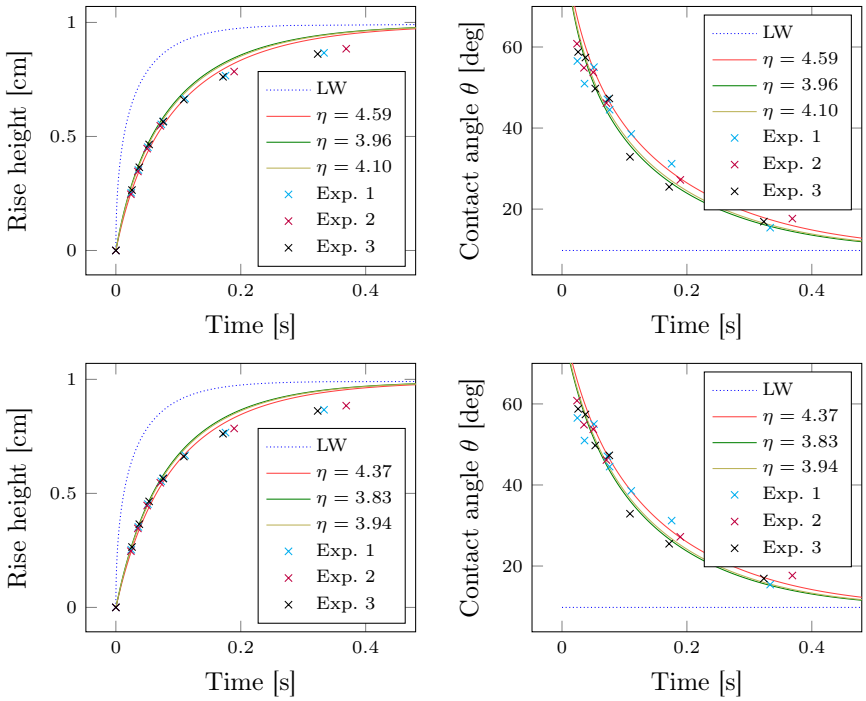

Figure B.10: Simulation results of the Lucas-Washburn model (LW) and of the fitted upscaled (*top row*) and extended (*bottom row*) models for the Soltrol 170 experiments at radius $R = 0.65$mm. Red: h-fit; Green: θ-fit; Yellow: both-fit.

R [mm] (fit)		Upscaled η	Upscaled χ^2_ν	Upscaled η	Upscaled λ	Upscaled χ^2_ν	Extended η	Extended χ^2_ν	Extended η	Extended λ	Extended χ^2_ν
0.375	(h)	0.451	0.558	1.017	0.288	0.051	0.162	0.058	0.329	0.043	0.023
0.375	(θ)	0.414	1.981	0.414	5e-11	2.013	0.377	2.054	0.377	1e-11	2.088
0.375	(b)	0.416	1.252	0.413	0.016	1.244	0.367	1.143	0.357	0.045	1.041
0.5	(h)	0.924	2.433	2.081	5*	0.222	0.111	0.153	0.548	0.123	2.7e-3
0.5	(θ)	0.605	2.599	0.516	0.683	1.349	0.498	0.037	0.498	7e-11	0.039
0.5	(b)	0.637	2.738	0.637	4e-3	2.767	0.476	2.249	0.463	0.070	2.039
0.65	(h)	4.036	1.147	5.228	5*	0.436	2.849	0.234	3.334	0.149	0.197
0.65	(θ)	1.488	3.524	1.461	0.248	3.232	1.052	4.595	1.052	6e-12	4.683
0.65	(b)	1.907	6.552	1.907	7e-10	6.612	1.248	4.203	1.248	7e-10	4.242

*) Maximal allowed value in the fitting procedure, to avoid unphysically large slip lengths.

Table B.6: The dynamic coefficient η, slip length λ and reduced residuals χ^2_ν for the different fits (h: height, θ: contact angle, b: both) of the upscaled and extended models, for the water experiments.

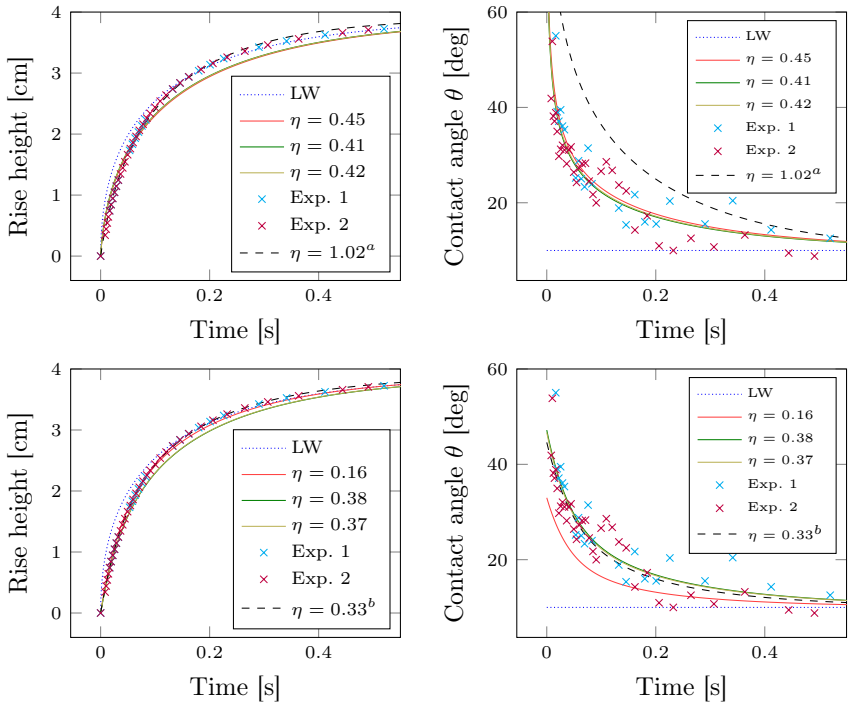

Figure B.11: Simulation results of the Lucas-Washburn model (LW) and of the fitted upscaled (*top row*) and extended (*bottom row*) models for the water experiments at radius $R = 0.375$mm. Red: h-fit; Green: θ-fit; Yellow: both-fit. Black dashed: h-fit including slip (a: $\lambda = 0.29$, b: $\lambda = 0.04$).

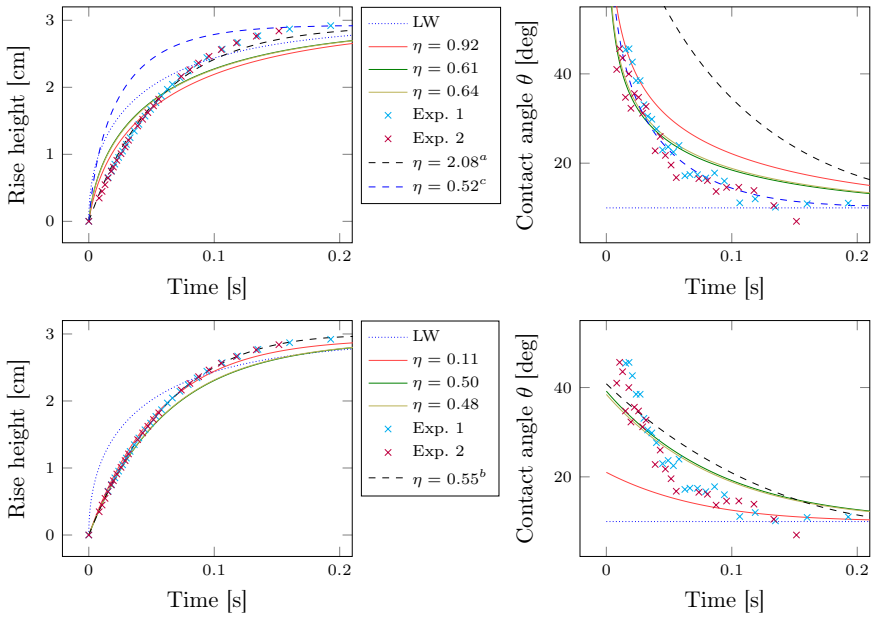

Figure B.12: Simulation results of the Lucas-Washburn model (LW) and of the fitted upscaled (*top row*) and extended (*bottom row*) models for the water experiments at radius $R = 0.5$mm. Red: h-fit; Green: θ-fit; Yellow: both-fit. Black dashed: h-fit including slip (a: $\lambda = 5$, b: $\lambda = 0.12$). Blue dashed: θ-fit including slip (c: $\lambda = 0.68$).

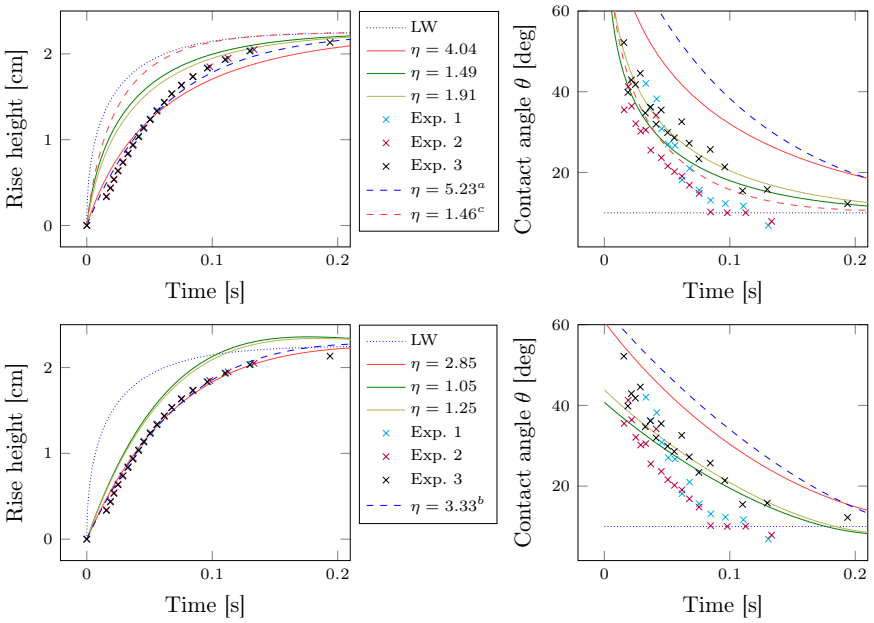

Figure B.13: Simulation results of the Lucas-Washburn model (LW) and of the fitted upscaled (*top row*) and extended (*bottom row*) models for the water experiments at radius $R = 0.65$mm. Red: h-fit; Green: θ-fit; Yellow: both-fit. Blue dashed: h-fit including slip (a: $\lambda = 5$, b: $\lambda = 0.15$). Red dashed: θ-fit including slip (*c*: $\lambda = 0.25$).

UHasselt Computational Mathematics Preprint Series

2021

UP-21-07 *S.B. Lunowa, A. Mascini, C. Bringedal, T. Bultreys, V. Cnudde, I.S. Pop*, **Dynamic effects during the capillary rise of fluids in cylindrical tubes**, 2021

UP-21-06 *J. Chouchoulis, J. Schütz, J. Zeifang*, **Jacobian-free explicit multiderivative Runge-Kutta methods for hyperbolic conservation laws**, 2021

UP-21-05 *L. von Wolff, I.S. Pop*, **Upscaling of a Cahn–Hilliard Navier–Stokes Model with Precipitation and Dissolution in a Thin Strip**, 2021

UP-21-04 *M. Bastidas Olivares, S. Sharmin, C. Bringedal, I.S. Pop*, **A numerical scheme for two-scale phase-field models in porous media**, 2021

UP-21-03 *M.J. Gander, S.B. Lunowa, C. Rohde*, **Non-overlapping Schwarz waveform-relaxation for nonlinear advection-diffusion equations**, 2021

UP-21-02 *M.J. Gander, S.B. Lunowa, C. Rohde*, **Consistent and asymptotic-preserving finite-volume domain decomposition methods for singularly perturbed elliptic equations**, 2021

UP-21-01 *J. Schütz, D. Seal, J. Zeifang*, **Parallel-in-time high-order multiderivative IMEX methods**, 2021

2020

UP-20-07 *M. Gahn, M. Neuss-Radu, I.S. Pop*, **Homogenization of a reaction-diffusion-advection problem in an evolving micro-domain and including nonlinear boundary conditions**, 2020

UP-20-06 *S.B. Lunowa, C. Bringedal, I.S. Pop*, **On an averaged model for immiscible two-phase flow with surface tension and dynamic contact angle in a thin strip**, 2020

UP-20-05 *M. Bastidas Olivares, C. Bringedal, I.S. Pop*, **An adaptive multiscale iterative scheme for a phase-field model for precipitation and dissolution in porous media**, 2020

UP-20-04 *C. Cancès, J. Droniou, C. Guichard, G. Manzini, M. Bastidas Olivares, I.S. Pop*, **Error estimates for the gradient discretisation of degenerate parabolic equation of porous medium type**, 2020

UP-20-03 *S.B. Lunowa, I.S. Pop, and B. Koren*, **Linearization and Domain Decomposition Methods for Two-Phase Flow in Porous Media Involving Dynamic Capillarity and Hysteresis**, 2020

UP-20-02 *M. Bastidas, C. Bringedal, and I.S. Pop*, **Numerical simulation of a phase-field model for reactive transport in porous media**, 2020

UP-20-01 *S. Sharmin, C. Bringedal, and I.S. Pop*, **Upscaled models for two-phase flow in porous media with evolving interfaces at the pore scale**, 2020